Strong field driven extreme nonlinear photoemission from individual single-walled carbon nanotubes

Mengxue Guan,[1,2,*] Lei Yan,[3] Shiqi Hu,[2,4] Yimin Zhang,[2,5] Daqiang Chen,[2,4] and Sheng Meng[2,4,6,†]
[1]*Centre for Quantum Physics, Key Laboratory of Advanced Optoelectronic Quantum Architecture and Measurement (Ministry of Education), School of Physics, Beijing Institute of Technology, Beijing 100081, China*
[2]*Beijing National Laboratory for Condensed Matter Physics and Institute of Physics, Chinese Academy of Sciences, Beijing 100190, China*
[3]*School of Physics and Information Technology, Shaanxi Normal University, Xi'an 710119, China*
[4]*School of Physical Sciences, University of Chinese Academy of Sciences, Beijing 100190, China*
[5]*Key Laboratory of Material Physics, Ministry of Education, School of Physics and Microelectronics, Zhengzhou University, Zhengzhou 450001, China*
[6]*Songshan Lake Materials Laboratory, Dongguan, Guangdong 523808, China*

(Received 30 October 2022; revised 27 December 2022; accepted 7 February 2023; published 21 February 2023)

Photoemission from nanostructures under strong fields has attracted significant interests in materials science and optoelectronic applications. Here, we report the extreme nonlinear photoemission in single-walled carbon nanotubes (SWCNTs) and its underlying mechanisms related to the microscopic carrier excitation and the sequential emission of occupied-state electrons. We show that the characteristic photoemission responses, e.g., nonlinear slope, of individual SWCNTs strongly depend on the unique electronic structures near the Fermi level, i.e., localization of the emitting states and their tunneling probabilities. The transition of photoemission mechanisms giving rise to the extreme nonlinear behavior was elucidated using Kohn-Sham potentials and the extended Fowler-Nordheim theory. This paper provides insights into photoemission dynamics of SWCNTs on the ultimate atomic length scale and attosecond time scale, will hopefully help design materials for tunable optoelectronic responses.

DOI: 10.1103/PhysRevB.107.075426

I. INTRODUCTION

Ultrafast control of electrons emitted from a nanoscale source continues to stay at the forefront of attosecond technologies [1,2]. It allows investigation of various ultrafast phenomena with an unprecedented precision including electron interference [3,4], high harmonic generation [5–7], real-time carrier motion, and ultrafast structure dynamics [8–10]. Electron photoemission takes place whenever the driving field is capable of inducing a bound-to-continuum transition, resulting in escaping of electrons from the target. When increasing the laser strength F, the predominant ionization mechanisms will transform from the perturbative multiphoton ionization [11] regime to the optical-field-emission (OFE) regime [12,13]. In the OFE regime, the photoemission process resembles field-controlled tunneling, thus the electron pulses, i.e., photoemission current (I), are synchronized to the waveform of incident light. This is of particular interest for practical applications, e.g., optical-phase detectors [14] and attosecond electron microscopy [15].

In addition to metal nanostructures [13,16–18], carbon nanotubes (CNTs) have emerged as a promising candidate for strong-field tunneling emission due to their extraordinarily high field enhancement and great stability [19–21]. Strong-field tunneling emission from CNTs has been identified for laser irradiation with a relatively short wavelength (410 nm), enabling the generation of photoelectron pulses with a low-energy spread (≈0.25 eV) [22]. Most recently, in one of our joint experimental and theoretical works, extreme strong-field photoemission with astounding nonlinearity ($I \propto F^{40}$) was reported in semiconducting single-walled carbon nanotubes (SWCNTs) after removing the metallic ones from the nanotube cluster by applying an aging process, and the nonlinearity depends on the band-gap width [23]. Although vertically aligned SWCNT clusters were used in the experiment, a few isolated, individual SWCNTs protruded out, which were believed to be the main emission sites [22]. Therefore, the results indicate that the electronic structure of SWCNTs provides a knob for controlling photoemission dynamics under the strong-field tunneling regime. A comprehensive understanding of the dependence of field-driven emission on underlying electronic properties is highly desirable for future applications in attosecond electronics and photonics, but is currently missing.

In this paper, we investigate the atomic-scale mechanism and real-time dynamics of photoemission from SWCNTs based on *ab initio* real-time time-dependent density functional theory (rt-TDDFT) [24–28]. We demonstrate that the tunneling currents in semiconducting and metallic SWCNTs show distinct temporal responses under strong laser pulses, i.e., the yield of current increases dramatically in semiconducting nanotubes when the laser field reaches its maximum strength, whereas it approaches saturation in metallic nanotubes. The astounding high nonlinearity in semiconducting SWCNTs is ascribed to the tunneling of electrons from electronic states

---

[*] Corresponding author: mxguan@bit.edu.cn
[†] Corresponding author: smeng@iphy.ac.cn

2469-9950/2023/107(7)/075426(9)

near the highest occupied states. However, the photoemission probabilities of those states are small in metallic nanotubes due to the synergistic effect of forbidden optical transition and the robust Kohn-Sham potentials resulting from the stronger screening effect. The above findings can be extended to more SWCNTs with different chiral indices for understanding their unique strong-field driven emission behaviors.

II. COMPUTATIONAL DETAILS

The TDDFT simulations are done in two main steps. First, ground-state information of SWCNTs is obtained based on DFT calculations, including the optimized atomic structures as well as corresponding electronic structures. Subsequently, real-time TDDFT is employed to perform accurate simulations of the interaction between laser fields and SWCNTs, which complements other contemporary approaches, e.g., solving the time-dependent Schrödinger equation numerically or analytically [29,30], and is one of the state-of-the-art methodologies. The *I-F* curves and the underlying electronic excitation-tunneling dynamics are revealed without any *a priori* assumptions. The detailed calculation processes are introduced as follows.

A. Structure and ground-state properties of SWCNTs

Ground-state DFT simulations were performed with SIESTA [31] using Troullier-Martins pseudopotentials in conjunction with the Perdew-Burke-Ernzerhof (PBE) functional [32]. The Brillouin zone (BZ) is sampled by the single $\boldsymbol{k}$ point with an energy cutoff of 100 Ry. The atomic structure of the tube was positioned in a cubic supercell with vacuum regions of $\approx$1.5 nm along three directions and fully relaxed until the force on each atom was less than 0.1 eV/nm.

Two representative finite-length SWCNTs are used in our calculations, i.e., an armchair (6, 6) metallic nanotube and a zigzag (10, 0) semiconducting nanotube, due to the fact that they have comparable geometries (e.g., diameter) and distinct electronic properties. Therefore, the photoemission dynamics are directly linked with the underlying electronic structures. Both of two SWCNTs are within the range of tube diameters in experiments and have comparable work functions of $\approx$4.4 eV [23]. For each SWCNT, one of the ends is capped while the other end is terminated by hydrogen atoms.

As for one-dimensional (1D) periodic carbon nanotubes, the $\boldsymbol{k}$ points are sampled on a uniform grid along the tube axis ($N_{\mathbf{k}} = 150$). We adopt a supercell geometry so that the tubes are aligned in a cubic array with the closest distance between adjacent tubes being 1.5 nm. At such a separation, the tube-tube interactions originated from the fictitious periodic images due to the imposing periodic boundary conditions are very small so that they can be treated as independent entities. In reality, when nanotubes are separated at a distance of nanometer scale, electrons can be favorably transported across tubes through electrical contacts and tunneling, which can even dictate the overall conductivity and thus the characteristics of CNT based emitters [33–36]. Deep understanding of the microscopic interactions among multitubes is also urgently needed for applications in conducting and sensing, which is beyond the scope of the present paper.

B. The interactions between laser fields and SWCNTs described by rt-TDDFT

In this paper, two codes within the framework of TDDFT are used, i.e., OCTOPUS [24,37] employing real-space-grids and TDAP [26,38] based on the local atomic basis. Both of them describe the laser-matter interactions in three-dimensional space $\boldsymbol{r}(x, y, z)$ via solving the time-dependent Kohn-Sham (KS) equation:

$$i\frac{\partial}{\partial t}\varphi_i(\boldsymbol{r}, t) = \left[-\frac{1}{2}\nabla^2 + V_{\mathrm{KS}}\right]\varphi_i(\boldsymbol{r}, t), \tag{1}$$

$$V_{\mathrm{KS}} = V_{\mathrm{ext}} + \sum V_I^{\mathrm{KB}} + \sum V_I^{\mathrm{local}} + V_H + V_{\mathrm{XC}}. \tag{2}$$

Here, $\varphi_i(\boldsymbol{r}, t)$ are the single-particle KS states (also called KS orbitals), V_{KS} is the Kohn-Sham potential, V_{ext} is the time-dependent external potential generated by a laser field, V_I^{KB} and V_I^{local} are the Kleinman-Bylander and local parts of the pseudopotential of atom I, and V_{XC} and V_H are the exchange-correlation (XC) and Hartree potentials, respectively. In our simulations, we use the length gauge to describe the interactions between the laser fields and modeled SWCNTs, where the vector and scalar potential of the field $E(t)$ are $\vec{A}(t) = 0$ and $V_{\mathrm{ext}} = -E(t)z$, respectively. The geometry effects on the field enhancement are considered in our simulations, and the localized field enhancement factor near the CNT tips is $\approx$14.6 [Fig. S1 in the Supplemental Material (SM) [39] (see also Refs. [40–55] therein)].

The applied external fields are polarized along the axial direction (coordinate z) of the SWCNTs, and are shaped as a Gaussian pulse:

$$E(t) = F\cos(\omega t)\exp\left[-\frac{(t - t_0)^2}{2\sigma^2}\right]. \tag{3}$$

Here, the width σ is 4 fs, $\hbar\omega = 3.02\,\mathrm{eV}$(i.e., $\lambda = 410\,\mathrm{nm}$), and the laser reaches the field maximum amplitude F at $t_0 = 15\,\mathrm{fs}$. The time- and space-dependent microscopic current density (Fig. S2 in the SM [39])

$$I(z, t) = -\frac{i\hbar}{2}\sum_i\{\varphi_i^*(z, t)\nabla\varphi_i(z, t) - \varphi_i(z, t)\nabla\varphi_i^*(z, t)\} \tag{4}$$

is integrated across a chosen plane that is perpendicular to the z direction with a distance of 0.2 nm from the cap of the nanotube:

$$I(t) = \int_s I(z, t)\cdot d\boldsymbol{S}. \tag{5}$$

The electronic kinetic spectra (Fig. S3 in the SM [39]) are obtained by taking the Fourier transform

$$I(\omega) = \int dt\, I(t)e^{i\omega t}. \tag{6}$$

Then, the maximum intensity of $I(\omega)$ is recorded with the increase of F.

Note that the photoemission yield depends on both the probability of electronic tunneling and the acceleration of emitted electrons. In the vicinity of the cap, the laser field and ionic potential field will compete with each other and electrons will oscillate back and forth. When the propagation distance increases and reaches a critical distance (>1 nm), ionic potential disappears and the liberated electrons will be driven by the laser field. Therefore, the accurate theoretical description of ionization current requires that the current detection surface stays far away from the cap, so that the bound and continuum states could be discerned [51,53,56]. In this paper, our study is limited to the investigation of the early stage of photoemission dynamics, i.e., electronic excitation and tunneling behaviors, due to the constraints of computer resources and the stability of computational algorithms [39].

III. RESULTS AND DISCUSSION

A. *I-F* curves related to the electronic structures of SWCNTs

For a single SWCNT, the emitted current density is highly sensitive to the atomic structure. In particular, for a capped SWCNT, it is believed that morphology of the tip will affect the strength and position of the peaks observed in density of states (DOS) spectra near the Fermi level (E_F) and electrons are sourced almost exclusively from the sharp nanotube tip [12,22], also as shown in Fig. 1(b) and Fig. S4 in the SM [39]. The calculated *I-F* curves and the corresponding electronic structures of two representative SWCNTs are shown in Figs. 1(c) and 1(d). Similar to the experimental results with photon energy of 1.55 eV [23], under moderate fields ($F < 3$ V/nm), the photoemission from the metallic nanotube is more significant. When $F > 3$ V/nm, saturation is observed in the metallic (6, 6) nanotube, whereas the current yield increases dramatically in the (10, 0) tube and becomes much higher than the metallic one. The semiconducting (10, 0) SWCNT shows an abrupt increase of nonlinear slope, i.e., $I \sim F^n$ from $n = 1.2$ to 5.3. We note that the nonlinear slope is marginally relevant to the laser frequency, while the photocurrent yields are enhanced due to the larger local-field intensities around the nanocap (Fig. S5 in the SM [39]). Due to the fact that the photocurrents are collected near the cap of the modeled SWCNTs, the nonlinear slope is underestimated [39].

B. Photoemission dynamics

To further reveal the dynamics of photoemission, we perform time-frequency analysis by means of the wavelet transform, which, comparing to $I(t)$, can additionally provide the energy information of microscopic current:

$$I_w(t_0, \omega) = \int I(t) w_{t_0,\omega}(t) dt = I_\omega(t), \tag{7}$$

with the wavelet kernel

$$w_{t_0,\omega}(t) = \sqrt{\omega} W[\omega(\mathrm{t} - \mathrm{t}_0)]. \tag{8}$$

The mother wavelet is given by the Gabor wavelet

$$W(x) = \frac{1}{\tau} \cos(x) e^{-x^2/2\tau^2}. \tag{9}$$

Figure 2 shows the results when the field amplitudes are 1 and 5 V/nm. It is clear that the energies of predominant electrons are centered around the laser photon energy, i.e., $\hbar\omega = 3.02$ eV, and the broadening is ≈1 eV. Higher-energy electrons with multiples of the fundamental energy ($n\hbar\omega_0$, where n is an integer) can also be generated via quiver motion, but with weaker strengths (Fig. S3 in the SM [39]). For a weak laser field (1 V/nm), currents from both nanotubes follow adiabatically to the electric field and the instantaneous yield in the (6, 6) tube is larger than in the (10, 0) tube, leading to the dominant contribution of the metallic nanotube [Figs. 2(a) and 2(b)]. However, under an intense field (5 V/nm), a sharp

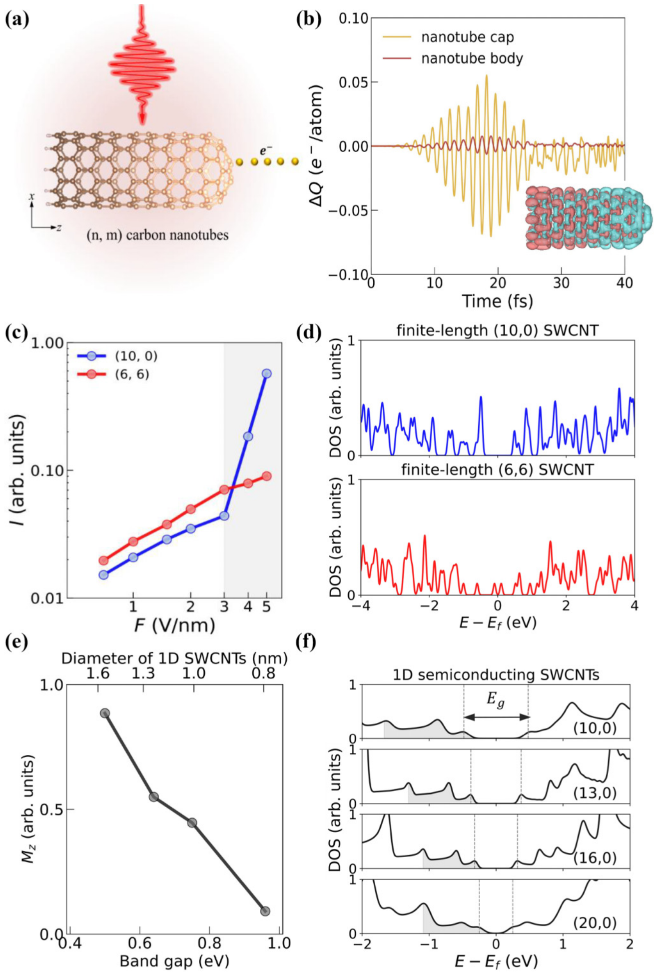

FIG. 1. (a) Schematic illustration of modeled SWCNTs irradiated by a linearly polarized laser pulse. (b) Dynamic charge evolution of a (10, 0) nanotube with the laser strength of 5 V/nm; here, $\Delta Q(t) = Q(t) - Q(0)$. The yellow and brown lines show the averaged contribution of the cap and body atoms. The inset shows the charge density differences of the (10, 0) nanotube when $t = 15$ fs. Here, the red and cyan colors represent the increase and decrease of charge density, respectively. (c) TDDFT computed *I-F* curves for the two typical SWCNTs illuminated under laser pulses with a wavelength of 410 nm and width of 4 fs. The gray shaded region represents the field amplitude range where the ultrahigh nonlinearity of photoemission occurs. (d) Normalized DOS spectra of finite-length (10, 0) and (6, 6) SWCNTs. (e) Optical transition probability of carriers located at the electronic states near the valence band maximum and its dependence on the band-gap width (E_g) and diameter of one-dimensional semiconducting SWCNTs. (f) DOS spectra of four representative semiconducting 1D SWCNTs. The gray shaded area in each panel indicates the energy range where the carrier excitation probabilities are included.

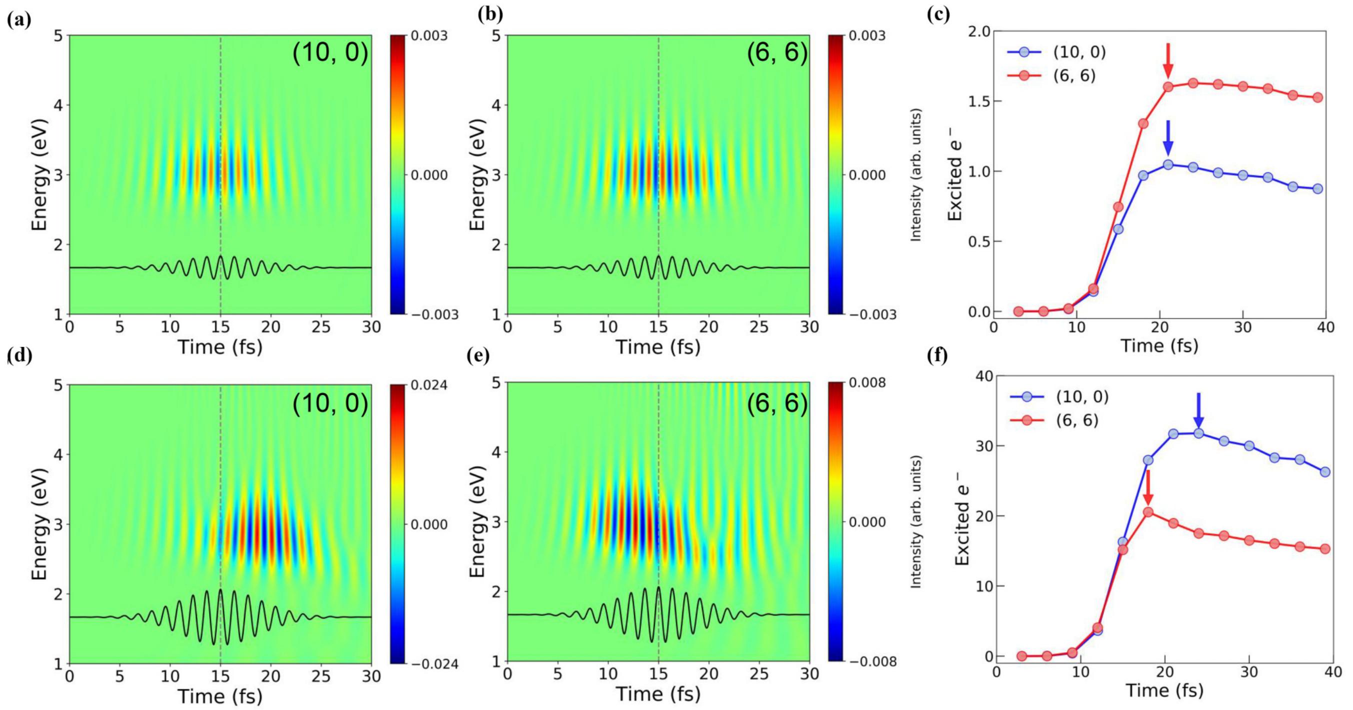

FIG. 2. Time-frequency analysis of microscopic currents in (a) (10, 0) and (b) (6, 6) nanotubes with $F = 1$ V/nm. The black line in each panel represents the laser waveform, which reaches its maximum strength at $t = 15$ fs, as indicated by the vertical dashed line. The positive and negative current represent the back and forth movement of the ionized electrons that are crossing the detection plane. (c) Time evolution of the number of excited electrons; the arrows are used to label the time that maximum carriers are excited. Panels (d)–(f) are analogous to panels (a)–(c), but are the results when $F = 5$ V/nm.

increase of tunneling current emerges in the (10, 0) tube when the laser reaches its maximum intensity at $t = 15$ fs [Fig. 2(d)]. In contrast, for the (6, 6) tube, most of current emission occurs before the peak [Fig. 2(e)], which indicates that most of the electrons have been depleted under the rather moderate laser fields and no extra electrons can contribute to photoemission even if stronger fields are applied. Based on that, the distinct performance of two SWCNTs shows that the instantaneous photoelectric responses under strong-field illumination are determined by whether there are plenty of electrons being excited and emitted from the nanotube.

The dependence of photoemission on electronic excitation is identified by calculating the number of excited electrons via projecting the time-evolved wave functions $[|\varphi_n(t)\rangle]$ on the basis of the ground-state Kohn-Sham orbitals $(|\psi_m\rangle)$:

$$\Delta n_e(t) = \sum_m^{\text{occ}} \sum_n^{\text{unocc}} |\langle\psi_m|S|\varphi_n(t)\rangle|^2, \tag{10}$$

where S is the overlap matrix expressed with numerical atomic-centered orbitals and all the unoccupied state electrons are summed up. Consistent with the above discussions, more electrons are promoted in the (6, 6) SWCNT during weak-field illumination [Fig. 2(c)], while the situation is reversed when the laser intensity surpasses the threshold for strong excitation in the (10, 0) SWCNT [Fig. 2(f)]. Meanwhile, the number of excited electrons maintains a continuous growth in the (10, 0) tube, rather than reaching saturation in the (6, 6) nanotube, indicating that the excitation mechanisms are different in these two types of SWCNTs.

To gain deeper insight into electronic dynamics under laser illumination, carrier excitations and potential subsequent electron emission at discrete KS levels are analyzed when the laser fields reach their maximum amplitudes ($t = 15$ fs). Figures 3(a) and 3(b) show the change of occupation numbers and the shape of the KS potential (V_{KS}) barrier for (10, 0) and (6, 6) SWCNTs, respectively. Under a weak field (1 V/nm), the energy intervals between the states that lose and gain electrons are equal to the incident photon energy (i.e., 3 eV). Meanwhile, though the KS potentials are bent down from the vacuum level (VAC), the barrier heights are only slightly decreased, indicating that the surface barrier is more steplike and tunneling is prohibited; therefore, multiphoton photoemission is dominant. For both two SWCNTs, the initial states that lose electrons are ≈2 eV below the Fermi energy, and it is expected that two or three photons are needed to overcome barriers with work functions ≈4.4 eV. In the (6, 6) SWCNT, most of the carriers are excited from the states close to the highest occupied molecular orbital (HOMO) at the single Γ point of the nanocluster. These localized states are closer to the VAC and have a larger tunneling probability than those in the (10, 0) SWCNT, resulting in a more significant current yield.

When F is larger than 3 V/nm, i.e., the threshold laser strength for the extreme nonlinearity, the V_{KS} is further bent around or even below HOMO level and electrons can be excited and emitted directly from occupied levels. In this regime, the tunneling probability increases for the higher occupied level, as it faces a narrower tunneling barrier. For the (10, 0) SWCNT, with the increase of laser strength, the high-

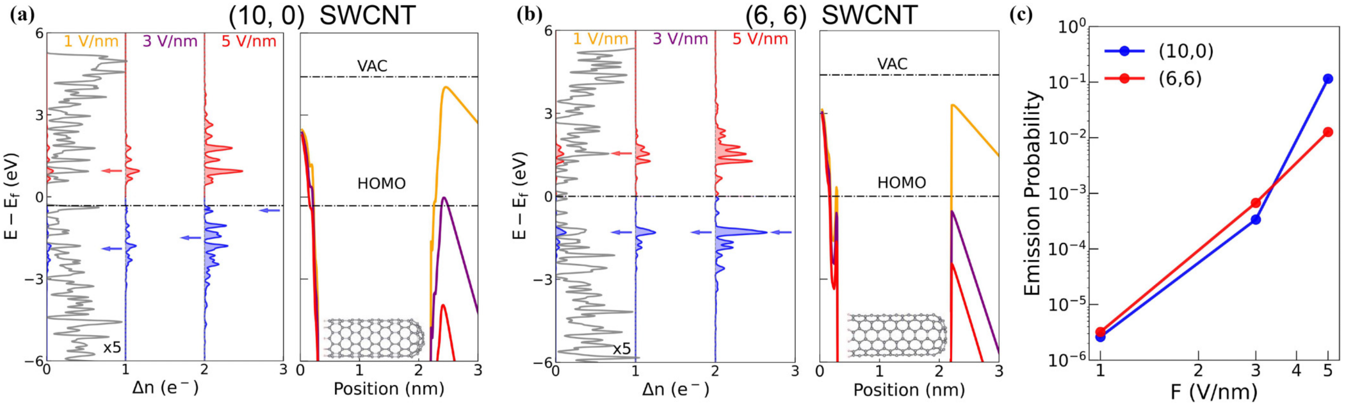

FIG. 3. (a), (b) Energy distributions of the excited electrons (red) and holes (blue) in (a) (10, 0) and (b) (6, 6) SWCNTs under the irradiation of three optical fields. The spatial-resolved KS potentials are shown in the right panels. The gray solid lines in panels (a) and (b) are the corresponding DOS spectra. The blue arrows indicate the highest occupied states that contribute to hole removal and the red arrows show the dominant localized states of excited electrons. (c) Emission probability of two SWCNTs based on the extended Fowler-Nordheim theory.

est occupied states that contribute to the tunneling excitation keep moving towards the HOMO level and the height of the KS potential barrier decreases linearly. Therefore, not only are more electrons excited, but also the tunneling probability grows, and both play important roles in introducing the ultrahigh nonlinearity of photoemission. In contrast, for the (6, 6) SWCNT, dominant excited states are pinned at the first van Hove singularity (vHS), and stronger field only leads to a weaker barrier bending, which might originate from the stronger screening effects in metallic nanotubes. Therefore, even though the current emission is enhanced, the emergence of ultrahigh nonlinearity is prohibited.

In order to obtain a quantitative description of the emission probability, a generalized Fowler-Nordheim (FN) theory is adopted, in which the energy band structure of SWCNTs has been taken into account [57–61]. To identify the validity of the FN model, Keldysh parameter was first calculated to estimate the magnitude of the optical field required to support quasistatic electron tunneling [62], given by $\gamma = \omega\sqrt{2m\Phi}/e\beta F$, where ω and F are, respectively, the frequency and maximum strength of the applied laser field, m is the mass of the electron and e is its charge, and β is the field enhancement factor of the emitting tips, i.e., $\beta \approx 14.6$. Φ is the ionization potential; for the carbon atom, $\Phi \approx 11.26$ eV. In this paper, when $F = 3$ V/nm, the calculated $\gamma \approx 1.18$. It has been frequently observed in solid surfaces and nanostructures that the transition to tunneling behaviors occurs when $\gamma \approx 2$ [13,22], reasonably supporting the field-driven photoemission regime.

The emission probability P_{em} is written as

$$P(t) = \frac{1}{N}\sum P(E,t), \tag{11}$$

$$P(E,t) = n(E)D(E,F(t)), \tag{12}$$

where $n(E)$ is the occupation number at energy level E shown in Figs. 3(a) and 3(b), and N is the total number of electrons. For an image charge barrier shown in Figs. 3(a) and 3(b), its height is reduced by the Schottky-barrier lowering effect [63], i.e., $V_{\text{KS}}(z,F) = V_0 - eFz - e^2/16\pi\varepsilon_0 z$, in which $-e^2/16\pi\varepsilon_0 z$ is the contribution from the image force and $-eFz$ is the contribution from the externally applied field, and the tunneling probability $D(E,F(t))$ can be estimated as

$$D(E,F(t)) = \frac{1}{1+\exp\left[\theta(E)\right]}, \tag{13}$$

$$\theta(E) = \frac{4\sqrt{2m}}{3\hbar F}(\Phi - E)^{\frac{3}{2}}v(y). \tag{14}$$

Here, $v(y) = 1 - y^2 + \frac{1}{3}y^2 \ln y$ and $y = \frac{\Delta\Phi}{\Phi}$ is the fractional lowering of the barrier [59]. e is the fundamental charge, m is the mass of a free electron in vacuum, $\hbar$ is the reduced Plank constant, Φ is the work function, and F is the applied laser amplitude. Consistent with the calculated *I-F* curves shown in Fig. 1(c), the P_{em} of the (6, 6) SWCNT is larger than that of the (10, 0) SWCNT for moderate laser fields, whereas under the intense laser the P_{em} in the (10, 0) SWCNT increases dramatically and shows an obvious "bending up" feature. The above results identify that photoemission in SWCNTs is dependent on the correlated excitation-tunneling dynamics, in which the unique electronic structures are vital in determining the macroscopic photoemission behaviors [64]. In the present paper, P_{em} at a representative moment ($t = 15$ fs) is discussed. To reveal the exactly time-dependent P_{em} during the whole photoemission dynamics, it is suggested to turn to models with solutions to oscillating barriers [30,65].

C. Carrier excitation behaviors with various chiral indices

The shape of the V_{KS} at the vaccum interface is one of the most delicate problems in the field emission theory, which is usually perturbed by various factors and beyond the scope of this paper [66,67]. Here, we focus on the investigation of distinct carrier excitation behaviors among different SWCNTs, which are identified to be determined by a unique combination of band structure and selection rules for optical transitions. Figures 4(a) and 4(b) show the energy distribution of the localized states (E_i) and the corresponding optical transition probabilities M_z of finite-length (6, 6) and (10, 0) SWCNTs, which is defined as

$$M_z^i(E_i) = \sum_f^{\text{unocc}} |\langle\varphi_f(E_f)|z|\varphi_i(E_i)\rangle|^2. \tag{15}$$

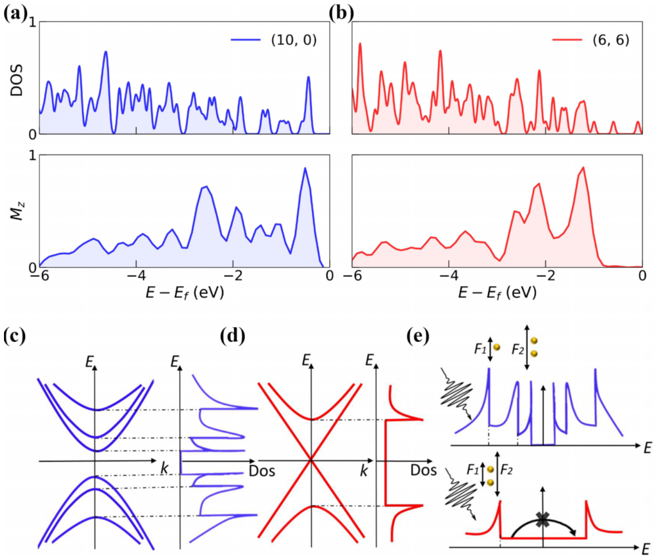

FIG. 4. Energy distribution of the localized occupied states and the corresponding optical transition probabilities M_Z for finite-length (a) semiconducting (10, 0) SWCNT and (b) metallic (6, 6) SWCNT. (c) Representative electronic energy-dispersion relations and density of states (DOS) of semiconducting 1D SWCNTs. (d) Representative electronic energy-dispersion relations and DOS of metallic 1D SWCNTs. (e) Schematic illustration of carrier excitation dynamics in the semiconducting (top) and metallic (bottom) SWCNTs under moderate (F_1) and intense (F_2, $F_2 > F_1$) optical fields. For semiconducting SWCNTs, the highest occupied states that contribute to the tunneling excitation keep moving towards the VBM with the increased laser strength. For metallic SWCNTs, the dominant excited states are pinned at the first vHSs due to the linear energy dispersion near the Fermi level.

Here, M_z^i represents the transition probability of the initial occupied state φ_i to all the unoccupied states φ_f under the laser pulse polarized along the z direction. To clarify the main tendency, Gaussian broadening is used to smooth the discrete data.

For both metallic and semiconducting SWCNTs, the maximum M_z^i is located at the van Hove singularity $\boldsymbol{k}$ points of the corresponding 1D SWCNTs (Fig. 4 and Fig. S7 in the SM [39]). Under the weak fields, the photon energy has determined the dominant tunneling states in semiconducting and metallic SWCNTs are far away and near the first vHS, respectively. When the laser pulses are strong enough to bend down the barrier, due to the fact that the M_z^i of those higher-energy electronic states is considerable in semiconducting SWCNTs, the carrier tunneling is realized by either indirect occupied-to-unoccupied-states tunneling or direct occupied-states tunneling.

For a metallic nanotube, however, though there are localized state distributions near the E_F, the optical transition between these states is approximately zero [68–70]. It arises from the discreteness of wave vectors along the circumference and the linear energy dispersion near the E_F. The 1D BZ of SWCNTs is expressed as the cutting lines of the two-dimensional BZ of the graphene layer. For armchair SWCNTs, the cutting lines will cross the K point of the hexagonal BZ and parallel to the nanotube axis, causing the touching of the two metallic bands at E_F. The dipole vector is nearly zero for transitions from an occupied metallic state to an unoccupied metallic state [68]. Therefore, in metallic nanotubes, the highest optically allowed occupied states are near the first vHS. As a result, carrier tunneling from the higher-occupied states can be achieved only if extremely intense fields are applied to bend the barrier below the corresponding energy levels, which might exceed the damage threshold. More discussions related to the nonlinear excitation dynamics in other finite-length SWCNTs are also provided in Fig. S6 in the SM [39].

The above findings can be extended to more SWCNTs and understand their unique strong-field driven carrier excitation behaviors. In reality, the lengths of the SWCNTs are usually longer than 10 μm, therefore the relative contribution of the nanotube body becomes predominant in carrier excitation, especially for those deep-level occupied states [71,72]. With the increase of tube length, the electronic structure of the tube body approaches that of the 1D SWCNT (Fig. S8 in the SM [39]). Based on the above analysis, 1D models are used to investigate the dependence of carrier excitation on the nanotube chirality, which will help to extend our results to more general cases and improve field-emission properties.

Here, four semiconducting 1D SWCNTs are taken as model systems, and the results are shown in Figs. 1(e) and 1(f). For the selected SWCNTs, the tube diameter varies from 7.83 Å [(10, 0) tube] to 15.66 Å [(20, 0) tube], and the corresponding band gap (E_g) between the two first vHSs decreases from 0.96 to 0.5 eV. For each 1D SWCNT, the transition probabilities of occupied states in the energy range from the third vHSs (3rd_vHSs) to the valence band maximum (VBM) are summed up, which is defined as

$$M_z = \sum_{i,\mathcal{E}_i > \text{3rd\_vHSs}}^{\mathcal{E}_i < \text{VBM}} M_z^i. \tag{16}$$

It is clear that M_z increases with the smaller band gap (larger tube diameter), indicating the larger possibilities for electronic excitation. Note that in the case of semiconducting SWCNTs with the diameter greater than or close to 1 nm, when the E_F is placed at the midgap, the work function decreases slightly with the diameter [73]. Therefore, in the VB-OFE regime, when assuming the same triangular shaped model of the potential energy barrier at the vacuum interface, the tunneling rate for the four kinds of 1D SWCNTs increase with the decrease of band-gap width, which cooperate with the larger optical transition probability and facilitate the highly efficient photoemission.

Based on the above analysis, we make a short summary about the characteristics that enable the abrupt increase of the I-F curve. First, the optical transition probabilities of the quantum states near the Fermi energy should be considerable; meanwhile, the decrease of the Kohn-Sham potential barrier should be sensitive to the external intense fields, so that the tunneling barrier can be bent below deeper occupied states, which will ensure the larger tunneling probabilities. Second, semiconducting SWCNTs with smaller band-gap width are suggested due to the larger possibilities for electronic tunneling.

It should be noticed that the macroscopic effects such as field enhancement factor (β) and propagation distance should also be carefully considered to obtain an accurate description and meaningful comparison among different samples. For example, the field enhancement of a SWCNT depends on its height and radius, which combine in an approximately multiplicative manner to determine the overall field enhancement factor of the nanotube [74]. Quantitative prediction of β has been proposed by some analytical approaches, including the line charge model [75] and the nonuniform axial line-charge model [76,77]. Assuming that the height of the SWCNTs is fixed, β is conventionally inversely proportional to its radius [78], and the stronger local fields of narrower SWCNTs will pose competition with the smaller tunneling probability in determining the experimentally detected current signals (e.g., nonlinear slope).

The deformed barrier with a lower height will also facilitate the potential thermionic emission, which is well understood on the basis of the Fermi-Dirac distribution [63]. Meanwhile, as electrons approach the apex to tunnel out, the nanotubes undergo Joule heating, leading to the broadened carrier distribution around Fermi level. Therefore, it is expected that a non-negligible thermal current will also contribute to the practical emission for realistic CNTs. In addition, due to the fact that approximate exchange-correlation potentials (e.g., adiabatic local density approximation and PBE) are used in the present paper, electron scatterings, e.g., electron-electron and electron-phonon scattering probabilities, might be underestimated [79]. The nonequilibrium electron scatterings and induced heating effect will lead to the increased quantum efficiency of photoemission and modified emission electron energy spectrum [65].

IV. CONCLUSIONS

In conclusion, *ab initio* rt-TDDFT simulations establish a straightforward relation of photoemission and the underlying excitation-tunneling dynamics in single SWCNTs. Under strong fields, the distinct photoemission behaviors among SWCNTs are closely related to their unique electronic structures near the Fermi level. In metallic nanotubes, the excitation of high-energy occupied states and the violent potential barrier bending are forbidden due to the linear energy dispersion and strong screening effect, respectively, both of which are necessary for the emergence of the ultrahigh nonlinearity if optical damages can be avoided. For semiconducting ones, the optical transition rate is inversely proportional to band-gap width, indicating that a larger field emission yield is expected from narrow band-gap SWCNTs. Our paper provides insight into the inherent correlation between the macroscopic photoemission performance and the microscopic atomic and electronic properties, which will hopefully help design materials for tunable optoelectronic responses.

ACKNOWLEDGMENTS

We acknowledge partial financial support from the National Natural Science Foundation of China (Grants No. 11934003, No. 12025407, No. 91850120, and No. 11774396), National Key Research and Development Program of China (Grant No. 2016YFA0300902), and “Strategic Priority Research Program (B)” of Chinese Academy of Sciences (Grant No. XDB330301). M.G. acknowledges support from the Beijing Institute of Technology Research Fund Program for Young Scholars.

---

[1] D. J. Park and Y. H. Ahn, Ultrashort field emission in metallic nanostructures and low-dimensional carbon materials, Adv. Phys.: X **5**, 1726207 (2020).

[2] P. Dombi, Z. Pápa, J. Vogelsang, S. V. Yalunin, M. Sivis, G. Herink, S. Schäfer, P. Groß, C. Ropers, and C. Lienau, Strong-field nano-optics, Rev. Mod. Phys. **92**, 025003 (2020).

[3] H. Lichte and M. Lehmann, Electron holography: Basics and applications, Rep. Prog. Phys. **71**, 016102 (2007).

[4] P. A. Midgley and R. E. Dunin-Borkowski, Electron tomography and holography in materials science, Nat. Mater. **8**, 271 (2009).

[5] P. M. Paul, E. S. Toma, P. Breger, G. Mullot, F. Augé, P. Balcou, H. G. Muller, and P. Agostini, Observation of a train of attosecond pulses from high harmonic generation, Science **292**, 1689 (2001).

[6] S. Ghimire and D. A. Reis, High-harmonic generation from solids, Nature Phys. **15**, 10 (2018).

[7] I. P. Christov, M. M. Murnane, and H. C. Kapteyn, High-harmonic Generation of Attosecond Pulses in the “Single-Cycle” Regime, Phys. Rev. Lett. **78**, 1251 (1997).

[8] E. Najafi, T. D. Scarborough, J. Tang, and A. Zewail, Four-dimensional imaging of carrier interface dynamics in pn junctions, Science **347**, 164 (2015).

[9] G. Herink, F. Kurtz, B. Jalali, D. R. Solli, and C. Ropers, Real-time spectral interferometry probes the internal dynamics of femtosecond soliton molecules, Science **356**, 50 (2017).

[10] S. Vogelgesang, G. Storeck, J. Horstmann, T. Diekmann, M. Sivis, S. Schramm, K. Rossnagel, S. Schäfer, and C. Ropers, Phase ordering of charge density waves traced by ultrafast low-energy electron diffraction, Nature Phys. **14**, 184 (2018).

[11] G. Mainfray and G. Manus, Multiphoton ionization of atoms, Rep. Prog. Phys. **54**, 1333 (1991).

[12] R. Bormann, M. Gulde, A. Weismann, S. V. Yalunin, and C. Ropers, Tip-Enhanced Strong-Field Photoemission, Phys. Rev. Lett. **105**, 147601 (2010).

[13] M. Krüger, M. Schenk, and P. Hommelhoff, Attosecond control of electrons emitted from a nanoscale metal tip, Nature (London) **475**, 78 (2011).

[14] F. Krausz and M. I. Stockman, Attosecond metrology: From electron capture to future signal processing, Nat. Photonics **8**, 205 (2014).

[15] M. T. Hassan, J. S. Baskin, B. Liao, and A. H. Zewail, High-temporal-resolution electron microscopy for imaging ultrafast electron dynamics, Nat. Photonics **11**, 425 (2017).

[16] P. t. Dombi, A. Hörl, P. t. Rácz, I. n. Márton, A. Trügler, J. R. Krenn, and U. Hohenester, Ultrafast strong-field photoemission from plasmonic nanoparticles, Nano Lett. **13**, 674 (2013).

[17] G. Herink, D. Solli, M. Gulde, and C. Ropers, Field-driven photoemission from nanostructures quenches the quiver motion, Nature (London) **483**, 190 (2012).

[18] W. P. Putnam, R. G. Hobbs, P. D. Keathley, K. K. Berggren, and F. X. Kärtner, Optical-field-controlled photoemission from plasmonic nanoparticles, Nature Phys. **13**, 335 (2016).

[19] F. Rossi and T. Kuhn, Theory of ultrafast phenomena in photoexcited semiconductors, Rev. Mod. Phys. **74**, 895 (2002).

[20] S. Zhou, K. Chen, M. T. Cole, Z. Li, J. Chen, C. Li, and Q. Dai, Ultrafast field-emission electron sources based on nanomaterials, Adv. Mater. **31**, 1805845 (2019).

[21] C. Li, X. Zhou, F. Zhai, Z. Li, F. Yao, R. Qiao, K. Chen, D. Yu, Z. Sun, and K. Liu, Quiver-quenched optical-field-emission from carbon nanotubes, Appl. Phys. Lett. **111**, 133101 (2017).

[22] C. Li, X. Zhou, F. Zhai, Z. Li, F. Yao, R. Qiao, K. Chen, M. T. Cole, D. Yu, and Z. Sun, Carbon Nanotubes as an ultrafast emitter with a narrow energy spread at optical frequency, Adv. Mater. **29**, 1701580 (2017).

[23] C. Li, K. Chen, M. Guan, X. Wang, X. Zhou, F. Zhai, J. Dai, Z. Li, Z. Sun, S. Meng, K. Liu, and Q. Dai, Extreme nonlinear strong-field photoemission from carbon nanotubes, Nat. Commun. **10**, 4891 (2019).

[24] X. Andrade, J. Alberdi-Rodriguez, D. A. Strubbe, M. J. Oliveira, F. Nogueira, A. Castro, J. Muguerza, A. Arruabarrena, S. G. Louie, and A. Aspuru-Guzik, Time-dependent density-functional theory in massively parallel computer architectures: The octopus project, J. Phys. Condens. Matter **24**, 233202 (2012).

[25] K. Lopata and N. Govind, Modeling fast electron dynamics with real-time time-dependent density functional theory: Application to small molecules and chromophores, J. Chem. Theory Comput. **7**, 1344 (2011).

[26] C. Lian, M. Guan, S. Hu, J. Zhang, and S. Meng, Photoexcitation in solids: First-principles quantum simulations by real-time TDDFT, Adv. Theory. Simul. **1**, 1800055 (2018).

[27] K. Uchida and K. Watanabe, Plasmon excitation and electron emission of a carbon nanotube under a linearly polarized laser: A real-time first-principles study, Phys. Rev. B **96**, 125419 (2017).

[28] J. A. Driscoll, S. Bubin, and K. Varga, Laser-induced electron emission from nanostructures: A first-principles study, Phys. Rev. B **83**, 233405 (2011).

[29] G. Z. Kiss, P. Foldi, and P. Dombi, Ultrafast plasmonic photoemission in the single-cycle and few-cycle regimes, Sci. Rep. **12**, 3932 (2022).

[30] Y. Luo, Y. Zhou, and P. Zhang, Few-cycle optical-field-induced photoemission from biased surfaces: An exact quantum theory, Phys. Rev. B **103**, 085410 (2021).

[31] J. M. Soler, E. Artacho, J. D. Gale, A. García, J. Junquera, P. Ordejón, and D. Sánchez-Portal, The SIESTA method for *ab initio* order-N materials simulation, J. Phys. Condens. Matter **14**, 2745 (2002).

[32] J. P. Perdew, K. Burke, and M. Ernzerhof, Generalized Gradient Approximation Made Simple, Phys. Rev. Lett. **77**, 3865 (1996).

[33] S. Banerjee, J. Luginsland, and P. Zhang, A two dimensional tunneling resistance transmission line model for nanoscale parallel electrical contacts, Sci. Rep. **9**, 14484 (2019).

[34] Q. W. Li, Y. Li, X. F. Zhang, S. B. Chikkannanavar, Y. H. Zhao, A. M. Dangelewicz, L. X. Zheng, S. K. Doorn, Q. X. Jia, D. E. Peterson, P. N. Arendt, and Y. T. Zhu, Structure-dependent electrical properties of carbon nanotube fibers, Adv. Mater. **19**, 3358 (2007).

[35] A. Buldum and J. P. Lu, Contact resistance between carbon nanotubes, Phys. Rev. B **63**, 161403(R) (2001).

[36] P. Zhang, J. Park, S. Fairchild, N. Lockwood, Y. Lau, J. Ferguson, and T. Back, Temperature comparison of looped and vertical carbon nanotube fibers during field emission, Applied Sciences **8**, 1175 (2018).

[37] X. Andrade, D. Strubbe, U. De Giovannini, A. H. Larsen, M. J. Oliveira, J. Alberdi-Rodriguez, A. Varas, I. Theophilou, N. Helbig, and M. J. Verstraete, Real-space grids and the Octopus code as tools for the development of new simulation approaches for electronic systems, Phys. Chem. Chem. Phys. **17**, 31371 (2015).

[38] S. Meng and E. Kaxiras, Real-time, local basis-set implementation of time-dependent density functional theory for excited state dynamics simulations, J. Chem. Phys. **129**, 054110 (2008).

[39] See Supplemental Material at http://link.aps.org/supplemental/10.1103/PhysRevB.107.075426 for details about the theoretical methods and other discussion.

[40] E. Runge and E. K. U. Gross, Density-Functional Theory for Time-Dependent Systems, Phys. Rev. Lett. **52**, 997 (1984).

[41] A. Castro, H. Appel, M. Oliveira, C. A. Rozzi, X. Andrade, F. Lorenzen, M. A. Marques, E. Gross, and A. Rubio, Octopus: A tool for the application of time-dependent density functional theory, Phys. Status Solidi B **243**, 2465 (2006).

[42] W. Ma, J. Zhang, L. Yan, Y. Jiao, Y. Gao, and S. Meng, Recent progresses in real-time local-basis implementation of time dependent density functional theory for electron-nucleus dynamics, Comp. Mater. Sci. **112**, 478 (2016).

[43] P. Song, P. Nordlander, and S. Gao, Quantum mechanical study of the coupling of plasmon excitations to atomic-scale electron transport, J. Chem. Phys. **134**, 074701 (2011).

[44] S. Berber, Y.-K. Kwon, and D. Tománek, Electronic and structural properties of carbon nanohorns, Phys. Rev. B **62**, R2291 (2000).

[45] P. Kim, T. W. Odom, J.-L. Huang, and C. M. Lieber, Electronic Density of States of Atomically Resolved Single-Walled Carbon Nanotubes: Van Hove Singularities and End States, Phys. Rev. Lett. **82**, 1225 (1999).

[46] A. De Vita, J.-C. Charlier, X. Blase, and R. Car, Electronic structure at carbon nanotube tips, Appl. Phys. A **68**, 283 (1999).

[47] D. L. Carroll, P. Redlich, P. M. Ajayan, J. C. Charlier, X. Blase, A. De Vita, and R. Car, Electronic Structure and Localized States at Carbon Nanotube Tips, Phys. Rev. Lett. **78**, 2811 (1997).

[48] P. Yaghoobi and A. Nojeh, Electron emission from carbon nanotubes, Mod. Phys. Lett. B **21**, 1807 (2007).

[49] M. Khazaei, A. A. Farajian, and Y. Kawazoe, Field Emission Patterns from First-Principles Electronic Structures: Application to Pristine and Cesium-Doped Carbon Nanotubes, Phys. Rev. Lett. **95**, 177602 (2005).

[50] M. F. Ciappina, J. A. Pérez-Hernández, A. S. Landsman, W. A. Okell, S. Zherebtsov, B. Förg, J. Schötz, L. Seiffert, T. Fennel, and T. Shaaran, Attosecond physics at the nanoscale, Rep. Prog. Phys. **80**, 054401 (2017).

[51] P. Wopperer, U. De Giovannini, and A. Rubio, Efficient and accurate modeling of electron photoemission in nanostructures with TDDFT, Eur. Phys. J. B **90**, 1307 (2017).

[52] N. Tancogne-Dejean, M. J. T. Oliveira, X. Andrade, H. Appel, C. H. Borca, G. L. Breton, F. Buchholz, A. Castro, S. Corni,

A. A. Correa, U. D. Giovannini, A. Delgado, F. G. Eich, J. Flick, G. Gil, A. Gomez, N. Helbig, H. Hübener, R. Jestädt, J. Jornet-Somoza, A. H. Larsen, I. V. Lebedeva, M. Lüders, M. A. L. Marques, S. T. Ohlmann, S. Pipolo, M. Rampp, C. A. Rozzi, D. A. Strubbe, S. A. Sato, C. Schäfer, I. Theophilou, A. Welden, and A. Rubio, Octopus, a computational framework for exploring light-driven phenomena and quantum dynamics in extended and finite systems, J. Chem. Phys. **152**, 124119 (2020).

[53] U. De Giovannini, A. H. Larsen, and A. Rubio, Modeling electron dynamics coupled to continuum states in finite volumes with absorbing boundaries, Eur. Phys. J. B **88**, 56 (2015).

[54] U. De Giovannini, H. Hubener, and A. Rubio, A first-principles time-dependent density functional theory framework for spin and time-resolved angular-resolved photoelectron spectroscopy in periodic systems, J. Chem. Theory Comput. **13**, 265 (2017).

[55] U. De Giovannini, G. Brunetto, A. Castro, J. Walkenhorst, and A. Rubio, Simulating pump-probe photoelectron and absorption spectroscopy on the attosecond timescale with time-dependent density functional theory, Chem. Phys. Chem. **14**, 1363 (2013).

[56] W. Wang, W. Yang, and Z. Li, Field electron emission imagesfar away from a semi-infinitely long emitter: A multi-scale simulation, J. Phys. Chem. C **122**, 27754 (2018).

[57] V. Filip, D. Nicolaescu, and F. Okuyama, Modeling of the electron field emission from carbon nanotubes, J. Vac. Sci. Technol. B **19**, 1016 (2001).

[58] K. L. Jensen, D. Finkenstadt, D. A. Shiffler, A. Shabaev, S. G. Lambrakos, N. A. Moody, and J. J. Petillo, Analytical models of transmission probabilities for electron sources, J. Appl. Phys. **123**, 065301 (2018).

[59] R. G. Forbes, Simple good approximations for the special elliptic functions in standard Fowler-Nordheim tunneling theory for a Schottky-Nordheim barrier, Appl. Phys. Lett. **89**, 113122 (2006).

[60] R. G. Forbes, Extraction of emission parameters for large-area field emitters, using a technically complete Fowler-Nordheim-type equation, Nanotechnology **23**, 095706 (2012).

[61] A. Mayer, N. M. Miskovsky, and P. H. Cutler, Theoretical comparison between field emission from single-wall and multi-wall carbon nanotubes, Phys. Rev. B **65**, 155420 (2002).

[62] L. V. Keldysh, Ionization in the field of a strong electromagnetic wave, Sov. Phys. JETP **20**, 1307 (1964).

[63] E. L. Murphy and R. H. Good, Thermionic emission, field emission, and the transition region, Phys. Rev. **102**, 1464 (1956).

[64] S. Miyauchi and K. Watanabe, Mechanism of electron excitation and emission from a nanoribbon under pulsed laser irradiation: Time-dependent first-principles study, J. Phys. Soc. Jpn. **86** 035003 (2017).

[65] Y. Zhou and P. Zhang, Quantum efficiency of photoemission from biased metal surfaces with laser wavelengths from UV to NIR, J. Appl. Phys. **130**, 064902 (2021).

[66] J.-M. Bonard, J.-P. Salvetat, T. Stöckli, W. A. de Heer, L. Forró, and A. Châtelain, Field emission from single-wall carbon nanotube films, Appl. Phys. Lett. **73**, 918 (1998).

[67] J. M. Bonard, J. P. Salvetat, T. Stöckli, L. Forró, and A. Châtelain, Field emission from carbon nanotubes: Perspectives for applications and clues to the emission mechanism, Appl. Phys. A **69**, 245 (1999).

[68] J. Jiang, R. Saito, A. Grüneis, G. Dresselhaus, and M. S. Dresselhaus, Optical absorption matrix elements in single-wall carbon nanotubes, Carbon **42**, 3169 (2004).

[69] E. H. Haroz, J. G. Duque, B. Y. Lu, P. Nikolaev, S. Arepalli, R. H. Hauge, S. K. Doorn, and J. Kono, Unique origin of colors of armchair carbon nanotubes, J. Am. Chem. Soc. **134**, 4461 (2012).

[70] S. Nanot, E. H. Haroz, J. H. Kim, R. H. Hauge, and J. Kono, Optoelectronic properties of single-wall carbon nanotubes, Adv. Mater. **24**, 4977 (2012).

[71] S. M. Yoon, J. Chae, and J. S. Suh, Comparison of the field emissions between highly ordered carbon nanotubes with closed and open tips, Appl. Phys. Lett. **84**, 825 (2004).

[72] R. Lv, F. Kang, D. Zhu, Y. Zhu, X. Gui, J. Wei, J. Gu, D. Li, K. Wang, and D. Wu, Enhanced field emission of open-ended, thin-walled carbon nanotubes filled with ferromagnetic nanowires, Carbon **47**, 2709 (2009).

[73] B. Shan and K. Cho, First Principles Study of Work Functions of Single Wall Carbon Nanotubes, Phys. Rev. Lett. **94**, 236602 (2005).

[74] T. E. Stern, B. S. Gossling, and R. H. Fowler, Further studies in the emission of electrons from cold metals, Proc. R. Soc. Lond. A **124**, 699 (1929).

[75] J. R. Harris, K. L. Jensen, and D. A. Shiffler, Modelling field emitter arrays using line charge distributions, J. Phys. D Appl. Phys. **48**, 385203 (2015).

[76] E. G. Pogorelov, A. I. Zhbanov, and Y. C. Chang, Enhancement factor, electrostatic force and emission current in a nanoneedle emitter, Europhysics Letters **85**, 17001 (2009).

[77] T. A. de Assis, F. F. Dall'Agnol, and R. G. Forbes, Field emitter electrostatics: A review with special emphasis on modern high-precision finite-element modelling, J. Phys. Condens. Matter **34**, 493001 (2022).

[78] J. Y. Huang, K. Kempa, S. H. Jo, S. Chen, and Z. F. Ren, Giant field enhancement at carbon nanotube tips induced by multistage effect, Appl. Phys. Lett. **87**, 053110 (2005).

[79] Y. Suzuki, L. Lacombe, K. Watanabe, and N. T. Maitra, Exact Time-Dependent Exchange-Correlation Potential in Electron Scattering Processes, Phys. Rev. Lett. **119**, 263401 (2017).